Design of an Improved Turbine Rim-Seal

James A Scobie, first author[1]
Department of Mechanical Engineering
University of Bath
Bath, BA2 7AY
United Kingdom
j.a.scobie@bath.ac.uk

Roy Teuber, second author
Siemens Industrial Turbomachinery Ltd.
Lincoln, LN5 7FD
United Kingdom
roy.teuber@web.de

Yan Sheng Lo, third author
Siemens Industrial Turbomachinery Ltd.
Lincoln, LN5 7FD
United Kingdom
yansheng.li@siemens.com

Carl M Sangan, fourth author
Department of Mechanical Engineering
University of Bath
Bath, BA2 7AY
United Kingdom
c.m.sangan@bath.ac.uk

Michael Wilson, fifth author
Department of Mechanical Engineering
University of Bath
Bath, BA2 7AY
United Kingdom
m.wilson@bath.ac.uk

Gary D Lock, sixth author
Department of Mechanical Engineering
University of Bath
Bath, BA2 7AY
United Kingdom

[1] Corresponding author information can be added as a footnote.

g.d.lock@bath.ac.uk

ABSTRACT

Rim seals are fitted in gas turbines at the periphery of the wheel-space formed between rotor discs and their adjacent casings. These seals, also called platform overlap seals, reduce the ingress of hot gases which can limit the life of highly-stressed components in the engine. This paper describes the development of a new, patented rim-seal concept showing improved performance relative to a reference engine design, using URANS computations of a turbine stage at engine conditions. The CFD study was limited to a small number of purge-flow rates due to computational time and cost, and the computations were validated experimentally at a lower rotational Reynolds number and in conditions under incompressible flow. The new rim seal features a stator-side angel wing and two buffer cavities between outer and inner seals: the angel-wing promotes a counter-rotating vortex to reduce the effect of the ingress on the stator; the two buffer cavities are shown to attenuate the circumferential pressure asymmetries of the fluid ingested from the mainstream annulus. Rotor disc pumping is exploited to reduce the sealing flow rate required to prevent ingress, with the rotor boundary layer also providing protective cooling. Measurements of gas concentration and swirl ratio, determined from static and total pressure, were used to assess the performance of the new seal concept relative to a bench-mark generic seal. The radial variation of concentration through the seal was measured in the experiments and these data captured the improvements due to the intermediate buffer cavities predicted by the CFD. This successful design approach is a potent combination of insight provided by computation, and the flexibility and expedience provided by experiment.

1. INTRODUCTION

Turbine rotor discs are among the most highly-stressed components in the engine, where metal temperatures must be limited to ensure acceptable-life, integrity

and reliability. A typical turbine stage is shown in Fig. 1, where rim seals are fitted at the periphery of the wheel-space between the turbine disc and its adjacent stator to reduce the ingress of hot mainstream gases. The ingress is principally caused by circumferential pressure asymmetries in the mainstream annulus, radially outward of the rim seal. A superposed sealing (purge) flow, bled from the compressor, is used to cool the rotor disc and to prevent, or at least dilute the ingress to a tolerable level. Superfluous use of this purge air can reduce the cycle efficiency and it is important to understand the fluid dynamics governing rim-seal performance.

The stationary vanes and rotating blades create an unsteady, three-dimensional distribution of pressure in the mainstream annulus near the seal clearance. *Ingress* of hot gas occurs in those circumferential regions of the clearance where the pressure in the annulus is higher than that in the wheel-space, and egress of sealing air occurs in those regions where this pressure difference is reversed.

There is a growing trend in industry to use unsteady computational fluid dynamics (CFD) codes to design rim seals and explore the mechanisms of ingress, e.g., [1][2]. Predictions of the unsteady, three-dimensional flows in both the annulus and wheel-space are however time-consuming and computationally expensive, and require significant expertise and insight. Experimental research is needed to validate the CFD results, including the use of turbine-based rigs running close to engine-operating conditions, e.g., [3]. There is also a requirement for detailed measurements made in simplified, more-flexible rigs specifically designed for instrumentation access in a more

benign environment; such rigs can offer an efficient and relatively inexpensive means of assessing new rim-seal design concepts.

This paper presents a design-concept study where CFD was used to create an improved rim seal operating at engine conditions ($Re_\phi \sim 10^7$, annulus Mach number ~ 0.65) with an engine vane and blade geometry. The numerical simulations were limited to just four purge-flow rates due to computational time and cost. The rim-seal concept was tested experimentally under incompressible flow conditions ($Re_\phi \sim 10^6$, annulus Mach number ~ 0.4) using the vane and blade geometries in the University of Bath single-stage turbine facility [4]. The test facility featured interchangeable rim-seal components offering flexibility and expediency in terms of data collection over a wide range of purge-flow rates. This enabled an efficient method of ranking and quantifying the performance of a wide range of generic and engine-specific seals, including the new seal concept developed from the CFD study. The experiments are thus used to inform design criteria that can be scaled to engine operating conditions through the use of theoretical models and CFD.

Section 2 is an overview of research groups currently studying ingress. Section 3 describes the new rim-seal concept. Section 4 describes the CFD model and the computational results. The experimental data are presented in Section 5, including details of the test facility and the rim seals investigated. Section 6 discusses the conclusions from this study.

2. LITERATURE REVIEW

A historical review of ingress has been provided by Sangan *et al*. [4] and this topic remains an important issue to gas-turbine designers. This Section reviews the most recent literature, with a focus on research groups conducting current work in this area. The rotational Reynolds number (see nomenclature) for the associated test facilities is given and it can be seen that the operating envelope of most steady-state rigs is typically an order of magnitude below engine conditions. There are clear advantages in experimenting near engine-representative Mach and Reynolds numbers; in practice it can be economical to operate in a more benign environment which lends itself to experimental detail and flexibility.

University of Aachen: $Re_\phi \sim 1.5 \times 10^6$

An experimental investigation of ingress into the upstream cavity of a 1.5 stage rig was conducted by Bohn *et al*. [5]. Unsteady two-dimensional Laser Doppler Anemometry measurements were reported, which mapped the velocity field found in the rim seal region. This showed the flow field was strongly influenced by both stator vanes and rotor blades. High pressure regions propagating upstream from the blades caused a local increase in ingress, even at large sealant flow rates.

Results of different numerical approaches were presented by Jakoby *et al*. [6] using data from the Aachen test rig for validation. A 360° simulation of the time-dependent flow field revealed large-scale structures also discovered in the experiments. When the sealant flow rate was small enough, low-pressure zones, which rotated at ~ 80% of the rotor speed, were found to strongly influence the ingress. The CFD

significantly under predicted the degree of ingress, though the 360° model (rather than a restricted sector model) produced results closer to experiment.

University of Sussex: $Re_\phi \sim 2 \times 10^6$

Eastwood *et al*. [7] investigated re-ingestion of sealant flow in a two-stage turbine stator-well rig at the University of Sussex. The test facility was developed to study the interaction of stator-well cooling and main-annulus air. Gas concentration measurements showed the amount of egress re-ingested into the downstream wheel-space was approximately 7% for the engine-representative sealing flow rates tested. The amount of re-ingestion reduced with increasing sealing flow. This rig has also been extensively used to study heat transfer in turbine hub cavities e.g., Dixon *et al*. [8].

Arizona State University: $Re_\phi \sim 0.6 \times 10^6$

Experimental measurements in a low-speed one-stage turbine rig were published by Zhou *et al*. [9]. Three rim-seal configurations were tested, including a double seal, to determine the influence of seal geometry on main gas path ingestion. The instantaneous fluid-velocity field was mapped using PIV at multiple circumferential positions; CO_2 gas concentration was used to determine the effectiveness. At low sealant flow rates, the measured radial- and tangential-velocity components identified areas where ingress and egress occurred. An unsteady, three-dimensional, sector CFD model under-predicted ingress, as the circumferentially rotating low pressure zones, predicted by the 360° simulations, could not be captured.

Wang *et al*. [1] performed numerical simulations using a 360° time-dependent approach, based on the ASU rig geometry with a radial and axial clearance seal. This work was extended by Mirzamoghadam *et al*. [2]. Circumferential distributions of ingress and egress rotating at the rotor speed were identified at lower sealant flow rates where ingress was significant. The periodicity of these distributions was not associated with the numbers of vanes or blades. At higher sealant flow rates, where little ingress occurs into the stator boundary layer, it was found the velocity distribution was associated with the blade pressure field. Note that the computations in this paper were performed at practical engine-operating conditions where the ingress is relatively small, and a sector model is expected to capture all significant effects present in a 360o model.

GE Global Research Centre: $Re_\phi \sim 3.5 \times 10^6$

Palafox *et al*. [3] discussed a new 1.5 stage hot gas ingestion rig designed to operate at near engine conditions, including representative Mach and Reynolds numbers. This rig has the capability of providing CO_2 gas concentration data, as well as unsteady pressure and temperature measurements. CFD validation of the preliminary rig data was documented by Ding *et al*. [10].

Penn State University: $Re_\phi \sim 1 \times 10^7$

Most recently, Barringer *et al*. [11] presented the design of a new 1.5 stage gas turbine research facility containing engine-representative hardware. This impressive facility will operate in a continuous, steady-state, high-pressure flow environment

approaching engine conditions. Future experiments will simulate the aerodynamic and thermal flow-field interactions between the mainstream gas path and the egress.

University of Bath: Re_ϕ ~ 1 x 10^6

The single-stage test facility at the University of Bath which features in this study was first presented by Sangan *et al*. [4]. The rig has been the focus of an extensive ingress research programme and is described in detail in Section 5. The test facility features interchangeable rim-seal components allowing a wide range of generic and engine-specific seal concepts to be tested. Most recently, Sangan *et al*. [12] investigated the feasibility of a finned turbine rim seal design. Measurements of gas concentration, pressure and swirl ratio were used to show the fins improved the seal performance.

Governing non-dimensional parameters for ingress

The ingress of fluid through the rim seal is an inertial phenomenon driven by differences in pressure, whereas the flow inside the wheel-space is controlled by the boundary-layers on the rotor and stator. Defined below are two non-dimensional flow rates (Φ_0 and λ_T) which respectively govern these inviscid and viscous phenomena. The sealing flow parameter, Φ_0, combines the effects of $C_{w,0}$, G_c and Re_ϕ into a single variable:

$$\Phi_o = \frac{C_{w,o}}{2\pi G_c \, \mathrm{Re}_\phi} = \frac{U}{\Omega b} \tag{1}$$

where U is the bulk mean radial velocity of sealing air through the seal clearance. As both Re_ϕ and $C_{w,0}$ include viscous terms which cancel, Φ_0 is therefore an inertial

parameter. The symbols are defined in the nomenclature and the reader is referred to Owen [13] for a detailed discussion of the so-called *effectiveness equations* which express the sealing effectiveness in terms of Φ_0.

Within the wheel-space, boundary layers will develop over both the rotating and stationary surfaces. At the rotor surface, fluid is accelerated to the disc speed by friction and pumped centrifugally. This phenomenon is often referred to as disc-pumping. On the stationary surfaces the tangential velocity decreases to zero near the wall and the radial pressure gradient causes a radial inflow.

The swirl ratio of the fluid in the inviscid core between the boundary layers in the wheel-space is defined as

$$\beta = \frac{V_\phi}{\Omega r} \tag{2}$$

where V_ϕ is the tangential component of velocity in the core. The swirl ratio controls the radial distribution of static pressure in the wheel-space. In a rotating inviscid fluid, the radial component, and the axial *gradients* of the axial and tangential components, of velocity must be zero [14]. All radial flow occurs inside the boundary layers, and the value of β adjusts to satisfy the continuity of the flow rate in the boundary layers.

The structure of the flow in the wheel-space is determined by the turbulent flow parameter (governing a viscous phenomenon), which is defined as

$$\lambda_T = C_{w,0}\,\mathrm{Re}_\phi^{-0.8} \tag{3}$$

For the free disc, where there is no stator, the entrained flow rate is characterized by $\lambda_T \approx 0.22$. It follows from Eqs. (1) and (3) that

$$\lambda_T = 2\pi G_c \, \mathrm{Re}_\phi^{0.2} \, \Phi_o \qquad (4)$$

3. NEW RIM-SEAL CONCEPT

Figure 2 illustrates the rim-seal geometries which were investigated computationally. Figure 2(a) shows the reference design to which the performance of the improved rim seal concept (b) was compared. This benchmark geometry, similar to that shown in Fig. 1, represents a typical double rim seal configuration found in current gas turbines. The new rim-seal concept will be simply referred to as the *angel-wing seal*.

An enlarged view of the angel-wing seal is shown in Fig. 3, which labels the outer-, intermediate- and inner-seal clearances and three corresponding wheel-spaces. The minimum radial clearance from the reference seal was maintained for the improved seal design. The essential differences between the new and reference seals are that the latter features (i) a stator-side angel wing, (ii) a relatively large outer wheel-space and (iii) an intermediate seal and wheel-space relatively close to the rotor surface. The intention of the angel wing is to create a mixing cavity to contain the hot ingress; the shape is designed to promote a counter-rotating vortex to reduce the effect of this ingress on the stator. The larger buffer volume in the outer wheel-space attenuates the circumferential pressure variation of the ingested fluid reducing the penetration of ingress to the intermediate wheel-space and highly-stressed rotor disc. The new seal concept takes advantage of the *disc pumping effect*: the sealing flow from the rotor boundary layer is pumped directly in the direction opposing the ingested flow, helping

to prevent ingress into the intermediate wheel-space while also providing cooling to the underside of the rotor blade platform.

Although not presented in this section, an iterative process was employed featuring five conceptual variations of the seal (see Section 5.2) before an improved geometry was established for the CFD calculations. This iterative process was possible using the flexible, expedient process in the experimental programme. Each variant was experimentally tested over a range of purge flow rates to identify improvements associated with a series of geometric changes. The final, patented geometry was designed to be practical for an industrial application while encompassing many of the beneficial features from the evolving concepts. The patented seal would be appropriate for different stages of the industrial turbine, and applicable for the first-stage of an aero-engine with axial assembly.

4. COMPUTATIONAL STUDY

4.1 Computational model

The CFD model used in this study consists of a stationary domain, involving three nozzle guide vanes in the mainstream annulus and a rotating domain with the rotor and five turbine blades - see Fig. 4(a). A sliding plane connecting the stationary and rotating domains was placed midway between the rim seal and the leading edge of the rotor blades. 7.5 million hexahedral elements were used to mesh the entire domain, with a J-grid and H-grid topology employed for the stationary and rotating domains respectively. Fig. 4(b) shows the mesh for the wheel-space domain with a $y^+_{ws} \approx 1$, a grid expansion

ratio between adjacent mesh cells of 1.3, and $y^+_{gp} \approx 10$ in the mainstream gas path. The commercial CFD code CFX v13 was used. The SST turbulence model was employed and the numerical methods used were the same as those described by Teuber *et al*. [15] with the exception of the time-step used here, which was 2.351×10^{-6} seconds.

The URANS computations were started from a frozen-rotor solution at engine representative conditions with $Re_\phi \approx 10^7$. Figure 5 shows the typical convergence behavior for a transient rim-seal computation with the computed sealing effectiveness monitored at four different positions; for clarity, these monitoring positions are also shown in Figure 4 (b). The vertical axis is $\varepsilon_{cc} = c_s / c_o$, the ratio of the stator concentration to that of the sealant: when $\varepsilon_{cc} = 1$ everywhere the wheel-space is sealed from ingress; and when $\varepsilon_{cc} = 0$ the wheel-space is entirely filled by ingress. Each unsteady simulation took up to four revolutions of the disc before the mixed out gas composition, consisting of the tracer gas and the ingested mainstream flow, was fully convected within the rim seal and the wheel-space. The solution was considered converged when a quasi-periodic behavior for the sealing effectiveness, static and total temperatures and pressures were obtained at selected monitoring points. The computations were performed with two HP Z800 workstations resulting in computational times of up to five weeks using 20 nodes in parallel.

4.2 Computational results

Computations were conducted at engine-representative conditions for a currently-operating Siemens engine with the associated vane, blade and wheel-space

geometries. The double radial-clearance seal (Fig. 2a) acted as the reference design. Due to the time available for the study, numerical simulations were restricted to just three sealing flow rates for this reference seal: Φ_0 = 0.065, 0.085 and 0.1; for the largest flow rate, the time-averaged value of $\varepsilon_{cc} \rightarrow 1$ on the stator at r/b = 0.96 (in-board of the angel wing) and the minimum flow rate to prevent ingress into the inner wheel-space was estimated to be $\Phi_{min} \sim 0.1$. Only a single computation was made for the angel-wing seal at Φ_0 = 0.072; relative to the reference seal, the time-averaged ε_{cc} was greater than those at both Φ_0 = 0.065 and 0.085. The CFD thus demonstrated that the improved design outperformed the reference case although insufficient data exists to quantify this improvement.

It should be noted that the experimental measurements using this inner-seal showed that $\Phi_{min} \sim 0.03$ - see Section 5. The measurements would not be expected to be *matched* by the CFD as the vane and blade geometries and the annulus flow conditions were different in the experiment and computations. Teuber *et al*. [14] discuss means of scaling Φ_{min} from rig to engine conditions. The computations carried out for the engine also include a small leakage flow into the outer wheel-space immediately beneath the stator platform.

4.3 Computational results for new rim-seal concept

Computational results for the angel-wing seal are described in this section. At the single purge flow rate tested, the inner wheel-space is nearly sealed, i.e. $\varepsilon_{cc} \rightarrow 1$ on the stator. While the time-averaged effectiveness is high in the outer and intermediate

wheel-spaces, there are maximum peaks of ingress and egress depending upon the unsteady pressure field in the annulus; this cyclic pressure field is governed by the relative position of the vanes and blades. Maximum ingress and egress occur when the superimposed pressure field above the rim-seal is, respectively, at a maximum or minimum relative to the wheel-space pressure. Figure 6 shows an instantaneous snap shot of (a) the computed velocity streamlines (b) the swirl ratio β and (c) the effectiveness for the case of maximum ingress. The case for the relative juxtaposition of vane and blade to create maximum egress is shown in Figure 7.

Consider Fig. 6a. The streamlines in the mainstream gas-path show fluid is ingested from near the surface of the stator hub in the annulus. Outside the stator boundary layer the swirl in the annulus is as high as β_a = 1.8 but decreases to zero near the stator wall (see Fig. 6b). The ingress with β < 1 is seen to migrate towards the stator-side of the seal lip and the highly-swirling flow (β > 1) down the rotor platform lip, before being ingested into the outer wheel-space. In the seal-gap region the effectiveness (see Fig. 6c) is nearly zero, *i.e.* the instantaneous gas temperatures would be near that in the annulus. A small amount of flow remains in the seal gap to form a clockwise-rotating vortex. Figure 6 illustrates the strength of the mixing between the ingested and sealant fluids through the outer seal, both in terms of concentration and swirl ratio. This implies a significant exchange of momentum and concentration between the two fluids.

The outer wheel-space acts as a buffer cavity to attenuate the variation in circumferential pressure which drives ingress further through the intermediate seal.

Here, this mixed-out ingress is directly opposed by the sealant flow which is pumped radially upwards by the rotating disc in the intermediate wheel-space. Within the seal clearance the sealing flow from the rotor boundary layer is pumped directly in the direction opposing this ingress, helping to prevent ingestion into the intermediate wheel-space. This boundary layer also provides cooling to the underside of the rotor-blade platform.

The shape of the angel wing helps to induce a counter- rotating vortex structure in the outer wheel-space. This is assisted by the minor leakage flow ejected from underneath the stator platform. Under conditions of maximum ingress, the fluid in this cavity is predominately ingested from the gas path. Fig. 6c shows the ingress migrates towards the center of the counter-rotating vortex; this ensures that the gas with the *highest temperature* does not directly contact the stator components.

Figure 7 shows an instantaneous snap shot of (a) the computed velocity streamlines, (b) the swirl ratio β and (c) concentration for the case of maximum egress. The streamlines in the outer wheel-space demonstrate the same counter-rotating vortex structure. Here this structure is predominately created by the sealing flow ejected through the clearance intermediate seal and the underside of the rotor platform. The majority of the sealing flow is expelled directly into the seal gap and the egress mixes with the mainstream the gas path.

Ideally, computations would have also been conducted at rig conditions and validated with experimental data. Due to time limitations, computations were carried out only at engine conditions. Computations using the same CFD sector model were

performed at the rig conditions by Teuber *et al*. [15] for generic-seal designs (not those used here) and good agreement between the CFD and experiments was presented.

5. EXPERIMENTAL STUDY

A series of rim sealing geometries, leading to the improved angel-wing seal were examined experimentally using the University of Bath single-stage gas-turbine test facility. This Section describes the facility, the seals tested and the experimental results.

5.1 Experimental facility

The steady-state experimental facility was constructed in 2008 and is described in detail by Sangan *et al*. [4]. The test section, shown in Fig. 8, features a turbine stage with 32 vanes and 41 blades. The blades were symmetric NACA 0018 aerofoils which avoid the necessity of a dynamometer; the ratio of the leading-edge diameter to chord-length was 0.0984. The diameter of the disc was 380 mm and the height of the annulus was 10 mm.

By means of an electric motor, the disc could be rotated up to speeds of 4000 rpm, providing a rotational Reynolds number, $Re_\phi = 1.1 \times 10^6$. Although this is typically an order-of-magnitude less than that found in gas turbines the turbulent flow structure in the boundary layers is principally governed by the turbulent flow parameter, λ_T, and depends only weakly on Re_ϕ [14]; hence the flow structure in the rig is considered to be representative of that found in the cooling systems of engines.

The vanes and blades in the annulus also produced a flow structure representative of those found in engines, albeit at lower Reynolds and Mach numbers. Table 1 shows the three design points used in the experiments: each design point created similar velocity triangles and non-dimensional pressure distributions (determined on the vane platform) in the annulus [4]. The flow exiting the vanes is virtually incompressible and near atmospheric pressure; the density, ρ, speed of sound, a, and air viscosity, μ, are determined from the static temperature and pressure measured inside the wheel-space on the stator at $r/b = 0.993$. At the design points, the distribution of effectiveness and swirl in the wheel-space was shown to be independent of Re_ϕ for all seals tested.

Sealing air was introduced into the wheel-space at a low radius ($r/b = 0.642$) through an inlet seal. In order to measure the degree of ingress, the sealing flow was seeded to a 1% level with a carbon dioxide tracer gas. The concentration of CO_2 was monitored at the entrance to the wheel-space, c_0, and in the unseeded upstream flow through the annulus, c_a. The variation of concentration c_s with radius ($0.55 < r/b < 0.993$) along the stator in the wheel-space was determined by sampling through 15 hypodermic tubes of diameter 1.6 mm. Two of these radial locations ($r/b = 0.958$ and 0.850) were used as reference monitoring points for the outer and inner wheel-spaces, respectively, for the seals described in Section 5.2. In all cases the gas was extracted by a pump, which delivered the samples to a dual channel infrared gas analyzer. The measurements were time averaged and the completion of a full radial traverse of concentration took approximately 20 minutes. The combined uncertainty of the

concentration measurements was +/- 0.015% of the measured value; a detailed uncertainty analysis is presented in the appendix. A second series of 15 taps, similar to the concentration taps, were used to determine the radial distribution of static pressure, p, on the stator. Seven complementary Pitot tubes in the wheel-space, aligned with the tangential direction, were used to measure the total pressure, p_T in the fluid core. The tangential component of velocity in the core at each of the seven radial locations was calculated from Bernouilli's equation:

$$V_\phi = \left[\frac{2(p_T - p)}{\rho} \right]^{1/2} \tag{5}$$

The estimated uncertainty in the measured values of V_ϕ were +/- 3%.

The *concentration effectiveness* ε_c is defined as

$$\varepsilon_c = \frac{c_s - c_a}{c_o - c_a} \tag{6}$$

where the subscripts *a*, *0* and *s* respectively denote the air in the annulus, the sealing air at inlet, and at the surface of the stator. For the experiments conducted here, c_a and c_0 were constants (approximately 0% and 1% respectively) and c_s varied with radius on the stator. In particular, $\varepsilon_c = 1$ when $c_s = c_0$ (zero ingress) and $\varepsilon_c = 0$ when $c_s = c_a$ (zero sealing flow). Note this definition is consistent with ε_{cc} as $c_a = 0$ in the computations.

5.2 Rim-seals investigated experimentally

Interchangeable 360° rim seals could be fitted to the periphery of the wheel-space, with both rotor- and stator-side features. These components were CNC machined from aluminum and were designed as scaled versions of those used in the engine. Seal

changes and re-alignment could be completed in a single working day. The experimental rig was specifically designed for this flexibility, providing relatively simple and expedient measurements over a full range of purge-flow rates and rotational speeds.

The improved angel-wing seal evolved from an iterative process using six variations of the seal geometry. The variations were created using a 360° angel wing mounted onto the stator and an insert, or combination of inserts, attached to the rotor and rotor-platform. This allowed an investigation of various radial-overlapping arrangements with the angel wing. The minimum clearance, $s_{c,rad}$ = 1.28 mm was maintained throughout the study. Sketches of the seal evolution from a bench-mark reference double seal (similar to that in Fig. 2a) through to the improved angel-wing seal (scaled from Fig. 2b) are shown in Fig. 9. Note the flow through the annulus is left to right. Full sets of data were collected for each variation over a range of sealant flow rates $0 < \Phi_0 < \Phi_{min}$ at the three design points - this data included the radial distribution of sealing effectiveness, pressure and swirl. Each geometric iteration created a marginal improvement in sealing performance in the outer, intermediate and inner wheel-spaces.

Detailed data is presented in the next section for the reference and the improved seals, i.e. seals (a) and (f) respectively in Figure 9. Schematic diagrams of these two rim seals (labelled *Reference* and *Angel Wing*) are shown in Figure 10 (a) and (b) and the static dimensions are given in Table 2. Concentration data was collected at 15 radial locations on the stator. For the angel-wing seal, two sampling taps were located within the angel-wing section to assess the variation in effectiveness through the outer, intermediate and inner wheel-spaces; these monitoring positions are shown in Fig.

10(c). Note that the discussion below will reference the outer, intermediate and inner rim seals and wheel-spaces as labeled in Fig. 3.

5.3 Radial variation of sealing effectiveness

Figure 11 shows the radial variation of concentration sealing effectiveness measured on the stator for both the reference and angel-wing seals. A thumb-nail sketch of the seals is included in this figure; it should be noted the external flow is from left to right (i.e. from the stator towards the rotor). The experiments were conducted at $Re_\phi = 8.2 \times 10^5$ at three consistent sealant flow rates (Φ_0 = 0.03, 0.05 and 0.07) between both cases; at this rotational Reynolds number, Φ_0 and λ_T are, coincidently, nearly equal in magnitude. Though not shown in the figure, the data is independent of Reφ at the three design points tested, as previously demonstrated by Sangan *et al*. [16] with a range of single- and double-clearance seals.

At all radii within the outer wheel-space ($r/b > 0.93$), the angel-wing seal provides an improved effectiveness over the reference seal. As expected, ε_c increases as Φ_0 increases. There is a dramatic increase in effectiveness from $\varepsilon_c = 0$ in the annulus, indicating mixing of the ingress and egress fluids through the outer rim seal. The concentration at the stator wall is determined by this mixed fluid, which enters the boundary layer and flows radially inward. For both seals the effectiveness is essentially constant in this outer wheel-space, suggesting that near-complete mixing has occurred in a region very close to the outer rim seal.

Between the outer and the inner ($0.65 < r/b < 0.85$) wheel-spaces there is a significant increase in effectiveness; the ingress is predominantly contained within the outer buffer volume. For the angel-wing seal, the effectiveness is seen to increase in two stages through the intermediate wheel-space ($0.85 < r/b < 0.95$) as predicted by the CFD.

For the angel-wing, the inner wheel-space is sealed ($\varepsilon_c = 1$) for all three sealing flow rates presented here. The inner wheel-space for the reference case is sealed at the higher two flow rates but not at $\Phi_0 = 0.03$. Again, ε_c is invariant with radius; the rapid increase at $r/b < 0.65$ is caused by the presence of the inlet seal where the sealing flow is introduced.

In the practical situation of an engine, the inner wheel-space could operate at an acceptably low metal temperature with the hot, ingested gas confined to the outer wheel-space protected by a more robust alloy.

5.4 Variation of sealing effectiveness with sealing flow

Figure 12 shows the variation of ε_c with Φ_0 for the angel wing seal measured at four monitoring locations. A thumb-nail sketch of the seal configuration showing these locations is included in this figure. At $\Phi_0 = 0.03$ the inner wheel-space is virtually sealed despite the outer wheel-space experiencing an effectiveness of ~ 50%. The data reveals that the intermediate seal limits the penetration of ingress into the intermediate wheel-space, as predicted by the CFD. The lower portion of this wheel-space features a stator-

rotor-stator labyrinth. This is shown to be an effective seal, inhibiting ingress into the inner wheel-space.

Also shown in Fig. 12 are comparisons between the experimental data and the theoretical variation of effectiveness according to the effectiveness equations originally presented by Sangan *et al*. [4]. The fit between these equations and the measured variation of ε_c with Φ_0 was optimized using the statistical model featuring maximum likelihood estimates described by Zhou *et al*. [17]. For all cases the experimental data is in good agreement with the theoretical curves.

The table inserted into Fig. 12 lists Φ_{min}', the value of Φ_0 required for ε_c = 0.95. The table shows that the flow rate required to seal the inner wheel-space to 95% is approximately a quarter of that required for the outer wheel-space; this demonstrates the virtue of the intermediate-cavity design. The measurements in the intermediate wheel-space have captured the features predicted by the CFD and it is encouraging to see the data support the concept behind the design of the seal discussed in Section 3.

Figure 13 shows a comparison between the reference and angel-wing seals. In both cases the effectiveness was determined in the inner wheel-space at r/b = 0.85 and in the outer wheel-space at r/b = 0.958. The data was collected at the three design points (see Table 1) and shown to be independent of Re_ϕ. The added complexity of the angel-wing geometry clearly provides an improved sealing performance over the full range of Φ_0 in *both* the inner and outer wheel-spaces. The improvement in Φ_{min}' is quantified in the table inserted into Figure 13.

Figure 9 illustrates the six (a–f) different seal configurations tested experimentally. Fig. 14(a) provides further detail from Fig. 13, illustrating the improvement in sealing performance in the inner wheel-space for the reference (a) and improved angel-wing (f) seals. Also shown are the intermediate marginal improvements associated with seal configurations (b) and (d), which represent the significant changes in the design evolution. As the four data sets are closely spaced, a detail of the highlighted region in Fig. 14(a) is shown in Fig. 14(b). The small improvements in Φ_{min}' for each configuration are shown in the Table inserted into Fig. 14(a).

The first iteration (b) incorporates the angel-wing stator-side feature of the improved geometry and the outer seal of the reference design. The data demonstrates a marginal improvement over the baseline case even in the absence of an inner seal feature. By incorporating the rotor attachment in seal (d), an inner overlap is formed and a further improvement in sealing performance is demonstrated. The most effective seal performance was achieved when all the iterative complex features were incorporated to form the double overlap inner seal found in the improved angel-wing design. Seals (c) and (e) produced similar results that fitted between the closely-spaced sets of data.

5.5 Radial variation of swirl ratio

Figure 15 illustrates the variation of swirl ratio β with non-dimensional radius for both the reference and angel-wing seals. The measurement locations for total pressure in the cores of the inner and outer wheel-spaces are shown for both seals. Once again

the data for both seals are shown for pairs of common superposed flow rates (λ_T = 0, 0.05 and 0.07) at Re_ϕ = 8.2 x 105, though the distribution of swirl has been shown to be independent of Re_ϕ at the three design points. The swirl ratio reduces dramatically from β_a = 1.8 in the annulus to β < 1 inside the outer wheel-space. This implies a rapid exchange of angular momentum through the outer rim-seal clearance.

For the case λ_T = 0, there is no superposed flow and the core rotation β = 0.44 is observed for r/b < 0.85, in accordance with Daily *et al*. [18]. The swirl in the outer wheel-space is seen to increase with the influence of highly swirling ingress. The case λ_T = 0 has maximum ingress and the concentration effectiveness everywhere in the wheel-space is zero. Increasing the sealing flow causes a reduction in the core rotation as the wheel-space is pressurized. The level of swirl at the periphery of the wheel-space also reduced as the increased sealant flow decreased ingestion from the annulus.

At common λ_T (i.e., common Φ_0) there are differences in the amount of ingress between the reference and angel-wing seals. Despite this, the swirl in the inner wheel-space for the two cases are similar, illustrating that β is governed principally by λ_T.

6. CONCLUSIONS

This paper presents a successful design approach where CFD was used to create a new, patented rim seal operating at engine conditions. The numerical simulations predicted an improved performance relative to a reference engine design, but the CFD was restricted to a small number of purge-flow rates due to computational time and cost. The new rim-seal concept was tested experimentally under incompressible flow

conditions. The test facility featured interchangeable rim-seal components offering flexibility and expediency in terms of data collection over a wide range of purge-flow rates and rotational speeds. An iterative process was employed featuring five conceptual variations of the seal before an improved geometry was established for the CFD calculations. Each variant was tested experimentally to identify improvements associated with a series of geometric changes. The final, patented geometry was designed to be practical for an industrial application while encompassing many of the beneficial features from the evolving concepts. This successful design approach is a potent combination of insight provided by computation, and flexibility and expedience provided by experiment.

The new rim seal features a stator-side angel wing and two buffer cavities between outer and inner seals: the angel-wing promotes a counter-rotating vortex to reduce the effect of the ingress on the stator; the two buffer cavities are shown to attenuate the circumferential pressure asymmetries ingested from the mainstream annulus. The disc-pumping effect is exploited to reduce the sealing flow rate required to prevent ingress, with the rotor boundary layer providing protective cooling.

Measurements of gas concentration, pressure and swirl were used to assess the performance of the new seal concept relative to a bench-mark reference seal at the University of Bath. The experiments measured the radial variation of concentration through the seal and the data captured the improvements through the intermediate buffer cavities predicted by the CFD.

DATA ACCESS STATEMENT

Due to confidentiality agreements with research collaborators, supporting data can only be made available to bona fide researchers subject to a non-disclosure agreement. Details of how to request access are available at the University of Bath data archive: http://dx.doi.org/10.15125/BATH-00116

FUNDING

The research described here is part of a Knowledge Transfer Partnership (KTP) programme jointly funded by the UK Technology Strategy Board and Siemens Industrial Turbomachinery Ltd. The experiments were supported by the Engineering and Physical Sciences Research Council (EPSRC).

NOMENCLATURE

a	*speed of sound (m/s)*
b	*radius of seal (m)*
c	*concentration of tracer gas (%)*
C_F	*flow coefficient (W/ Ωb)*
$C_{w,0}$	*nondimensional sealing flow rate (= $\dot{m}/\mu b$)*
G_c	*seal-clearance ratio (= $s_{c,ax}/b$)*
$\dot{m}$	*mass flow rate (kg/s)*
M	*Mach number*
p	*static pressure (Pa)*
p_T	*total pressure (Pa)*
r	*radius (m)*
Re_w	*axial Reynolds number in annulus based on radius (= $\rho W b/\mu$)*
Re_ϕ	*rotational Reynolds number (= $\rho \Omega b^2/\mu$)*
s_c	*seal clearance (m)*
U	*bulk mean radial seal velocity (= $\dot{m}_0/2\pi\rho b s_c$)*
V_ϕ	*tangential component of velocity (m/s)*
W	*axial velocity in annulus (m/s)*
β	*swirl ratio (= $V_\phi/\Omega r$)*
ε_c	*concentration effectiveness*

ε_{cc}	*computed concentration effectiveness (= c_s /c_0)*
Φ_0	*nondimensional sealing parameter (= $C_{w,0}/2\pi\, G_c\, \mathrm{Re}_\phi$)*
Φ_{min}	*minimum value of Φ_0 to seal wheel-space*
λ_T	*turbulent flow parameter (= $C_{w,0}\, \mathrm{Re}_\phi^{-0.8}$)*
μ	*dynamic viscosity (kg/ms)*
ρ	*density (kg/m3)*
Ω	*angular speed of rotating disc (rads/s)*

Subscripts

a	*annulus*
ax	*axial*
min	*minimum*
rad	*radial*
0	*sealing flow*
s	stator surface

REFERENCES

[1] Wang, C. Z., Mathiyalagan, S. P., Johnson, B. V., Glahn, J. A. and Cloud, D. F., 2012, "Rim Seal Ingestion in a Turbine Stage from 360-Degree Time-Dependent Numerical Simulations"; ASME J. Turbomach., **136**(3), 031007-1 to 12.

[2] Mirzamoghadam, A. V., Kanjiyani, S., Riahi, A., Vishnumolakala, R., and Gundeti, L., 2015, "Unsteady 360 Computational Fluid Dynamics Validation of a Turbine Stage Mainstream/Disk Cavity Interaction," ASME J. Turbomach., **137**(1), 011008-1 to 9.

[3] Palafox, P., Ding, Z., Bailey, J., Vanduser, T., Kirtley, K., Moore, K., and Chupp, R., "A New 1.5-Stage Turbine Wheelspace Hot Gas Ingestion Rig (HGIR) – Part I: Experimental Test Vehicle, Measurement Capability and Baseline Results"; ASME Paper GT2013-96020.

[4] Sangan, C. M., Pountney, O. J., Zhou, K., Wilson, M., Owen, J. M., and Lock, G. D., 2013, "Experimental Measurements of Ingestion through Turbine Rim Seals. Part 1: Externally-Induced Ingress," ASME J. Turbomach., **135**(2), 021012.

[5] Bohn, D. E. and Wolff, M., 2003, "Improved Formulation to Determine Minimum Sealing Flow - Cw, min – for Different Sealing Configurations," ASME Paper GT2003-38465.

[6] Jakoby, R., Zierer, T., Lindblad, K., Larsson, J., deVito, L., Bohn, D. E., Funcke, J., and Decker, A., 2004, "Numerical Simulation of the Unsteady Flow Field in an Axial Gas Turbine Rim Seal Configuration," ASME Paper No. GT2004-53829.

[7] Eastwood, D., Coren, D. D., Long, C. A., Atkins, N. R., Childs, P. R. N., Scanlon, T. J. and Guijarro-Valencia, A., 2012, "Experimental Investigation of Turbine Stator Well Rim Seal, Re-Ingestion and Interstage Seal Flows Using Gas Concentration Techniques and Displacement Measurements," ASME J. Eng. Gas Turb. Power, **134**(8), pp. 082501-1 to 9.

[8] Dixon, J. A., Guijarro-Valencia, A., Bauknecht, A., Coren, D. D., and Atkins, N. R., 2013, "Heat Transfer in Turbine Hub Cavities Adjacent to the Main Gas Path," ASME J. Turbomach., **135**, p.021025.

[9] Zhou, D. W., Roy, R. P., Wang, C. Z., and Glahn, J. A., 2011, "Main Gas Ingestion in a Turbine Stage for Three Rim Cavity Configurations," ASME J. Turbomach., **133**(3), 031023-1 to 12.

[10] Ding, Z., Palafox, P., Moore, K., Chupp, R., Kirtley, K., 2013 "A New 1.5-stage Wheelspace Hot Gas Ingestion Rig (HGIR) – Part II: CFD Modeling and Validation," ASME Paper GT2013-96021.

[11] Barringer, M., Coward, A., Clark, K., Thole, K. A., Schmitz, J., Wagner, J., Alvin, M. A., Burke, P., and Dennis, R., 2014, “The Design of a Steady Aero Thermal Research Turbine (START) for Studying Secondary Flow Leakages and Airfoil Heat Transfer,” ASME Paper GT2014-25570.

[12] Sangan, C. M., Scobie, J. A., Zhou, K., Wilson, M., Owen, J. M., and Lock, G. D., 2014, “Performance of a Finned Turbine Rim Seal,” ASME J. Turbomach., **136**(11), 111008 1 to 10.

[13] Owen, J.M., 2011, “Prediction of Ingestion Through Turbine Rim Seals---Part II: Externally Induced and Combined Ingress”; ASME J. Turbomach., **133**(3), 031006-1 to 9.

[14] Owen, J. M. and Rogers, R. H., 1989, Flow and heat transfer in rotating-disc systems, Volume 1: Rotor-stator systems, Taunton: Research Studies Press Ltd.

[15] Teuber, R., Wilson, M., Lock, G. D., Owen, J. M. Li, Y. S., and Maltson, J.D., 2013, “Computational Extrapolation of Turbine Sealing Effectiveness from Test Rig to Engine Conditions,” Proc. IMechE Part A: J. Power and Energy, **227**, 167-178.

[16] Sangan, C. M., Pountney, O. J., Scobie, J. A., Wilson, M, Owen, J.M., and Lock, G.D., 2013 “Experimental Measurements of Ingestion through Turbine Rim Seals. Part 3: Single and Double Seals,” ASME J. Turbomach., **135**(5), 051011-1 to 11.

[17] Zhou, K., Wood, S. N., and Owen, J. M., 2013, "Statistical and Theoretical Models of Ingestion through Turbine Rim Seals," ASME J. Turbomach., **135**(2), 021014-1 to 8.

[18] Daily, J. W., Ernst, W. D. and Asbendian, V. V., 1964, “Enclosed rotating discs with superposed through-flow: Mean steady and periodic unsteady characteristics of induced flow,” MIT Department of Civil Engineering, Hydrodynamics Laboratory Report No.64.

APPENDIX: UNCERTAINTY IN EFFECTIVENESS MEASUREMENTS

For convenience, the definition of sealing effectiveness (ε_c denoted here for simplicity as ε) given in Eq. 6 is repeated below:

$$\varepsilon = \frac{c_s - c_a}{c_o - c_a} \tag{A1}$$

where the subscripts *a*, *0* and *s* respectively denote the air in the annulus, the sealing air at inlet, and the surface of the stator.

Let δ_ε, δ_s, δ_0, δ_a be uncertainties in ε, c_s, c_0, c_a respectively so that

$$\begin{aligned} \varepsilon \pm \delta_\varepsilon &= \frac{c_s \pm \delta_s - (c_a \pm \delta_a)}{c_o \pm \delta_o - (c_a \pm \delta_a)} \\ &= \frac{(c_s - c_a)[1 + (\pm\delta_s \pm \delta_a)/(c_s - c_a)]}{(c_o - c_a)[1 + (\pm\delta_o \pm \delta_a)/(c_o - c_a)]} \end{aligned} \tag{A2}$$

$$= \varepsilon \frac{[1 + (\pm\delta_s \pm \delta_a)/(c_s - c_a)]}{[1 + (\pm\delta_o \pm \delta_a)/(c_o - c_a)]} \tag{A3}$$

If $(\pm\delta_0 \pm \delta_a) / (c_0 - c_a) \ll 1$ then

$$\varepsilon + |\delta_\varepsilon| \le \varepsilon \left\{ 1 + \frac{|\delta_s| + |\delta_a|}{c_s - c_a} + \frac{|\delta_o| + |\delta_a|}{c_o - c_a} \right\} \tag{A4}$$

Hence,

$$\frac{|\delta_\varepsilon|}{\varepsilon} \le \left\{ \frac{|\delta_s| + |\delta_a|}{c_s - c_a} + \frac{|\delta_o| + |\delta_a|}{c_o - c_a} \right\} \tag{A5}$$

If the uncertainty is a percentage of the full-scale range, which was the case in the experiments, then $\delta_s = \delta_0 = \delta_a = \delta$, say, and Eq. (A5) simplifies to

$$\frac{|\delta_\varepsilon|}{\varepsilon} \le 2\delta \frac{1 + \varepsilon^{-1}}{c_o - c_a} \tag{A6}$$

or

$$|\delta_\varepsilon| \le 2\delta \frac{1 + \varepsilon}{c_o - c_a} \tag{A7}$$

The average standard deviation, σ, in the range $0 < \varepsilon < 1$ can be calculated from Eq. (A7) by

$$\sigma = \frac{2\delta}{c_o - c_a} \sqrt{\int_0^1 (1 + \varepsilon)^2 d\varepsilon} = 3.06 \frac{\delta}{c_o - c_a} \tag{A8}$$

The CO_2 gas analyser had an overall uncertainty of 0.015% of each of its ranges. In the tests, where the 1% range was used, the concentration of gas in the sealing flow was close to the 1% range maximum. Hence $\delta / (c_0 - c_a) \approx 0.015$, and from Eq. (A8) it

follows that $\sigma \approx 0.046$. This value, which is an upper bound, exceeds the standard deviation found from the fitted $\Phi_0 - \varepsilon$ curves.

Figure Captions List

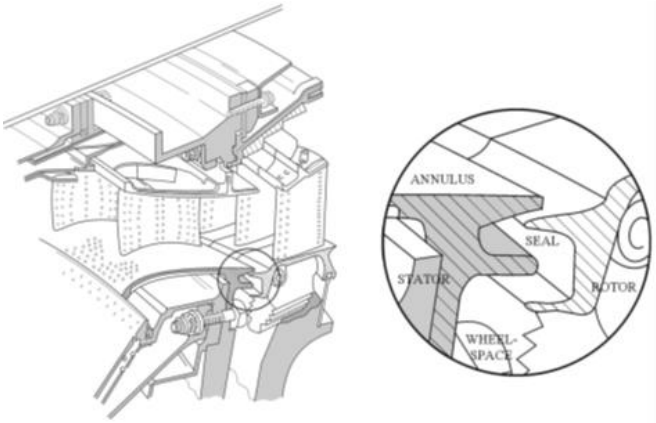

Fig. 1: (a) Typical high-pressure gas-turbine stage;
(b) detail of rim seal [4]

Fig. 2: Rim-seal concepts investigated by CFD: (a) reference seal (b) angel-wing seal

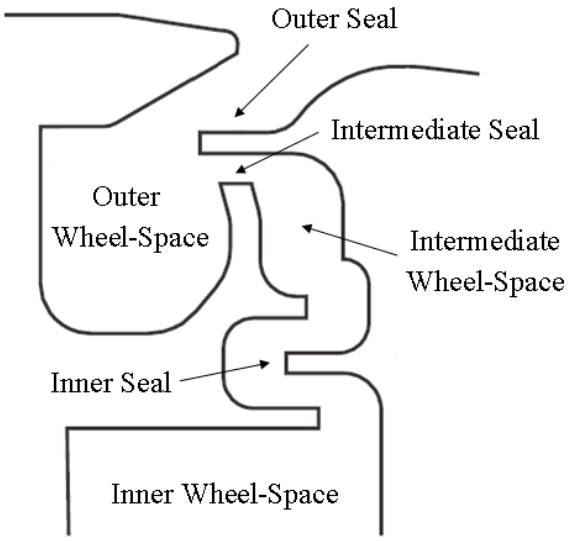

Fig. 3: Nomenclature for angel-wing seal

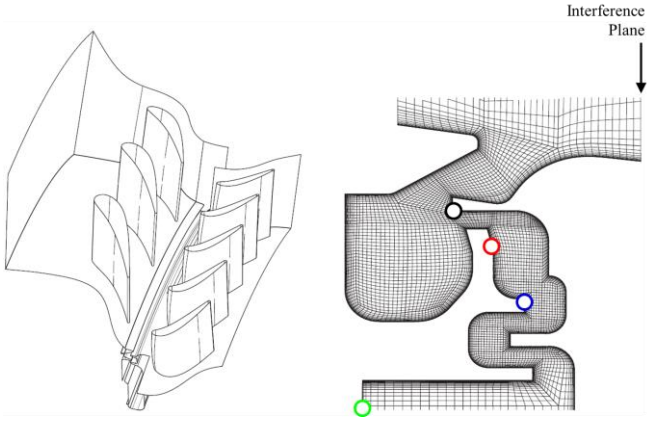

(a) (b)

Fig. 4: CFD model; (a) model domain; (b) wheel-space mesh

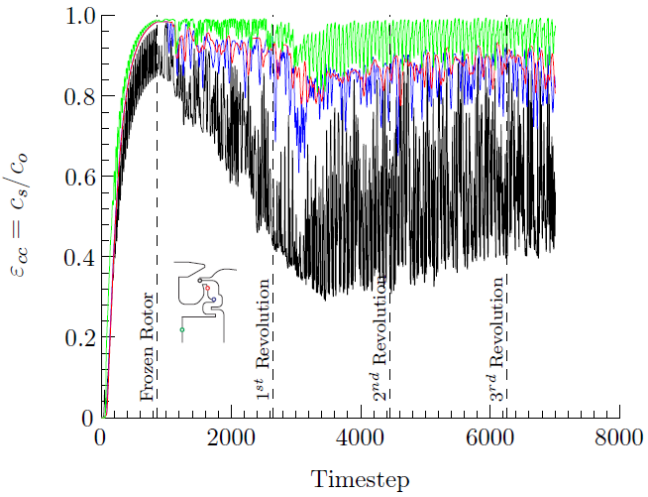

Fig. 5: Convergence behaviour for the sealing effectiveness ε_{cc} at four rim-seal positions

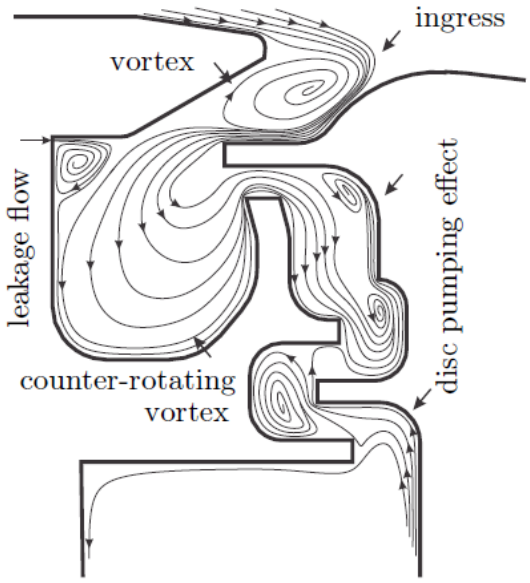

(a)

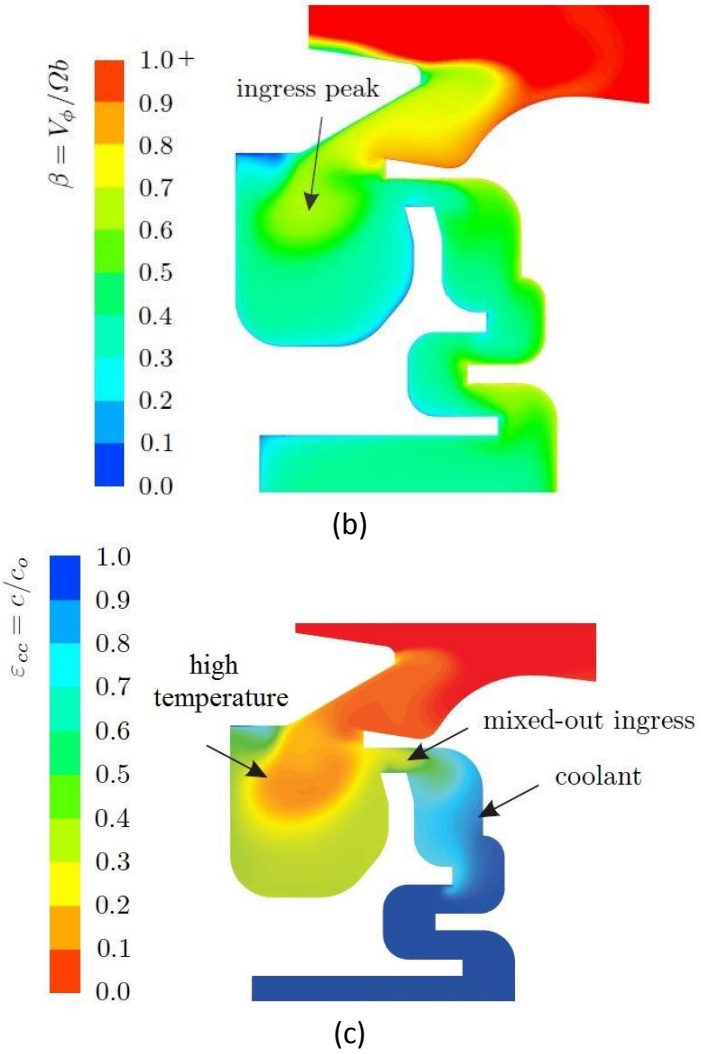

Fig. 6: Case of maximum ingress for improved seal design; (a) computed velocity stream lines; (b) contour plot with swirl ratio β – note, the swirl contours were limited to β = 1 despite β > 1 in the annulus; (c) contour plot of sealing effectiveness ε_{cc}

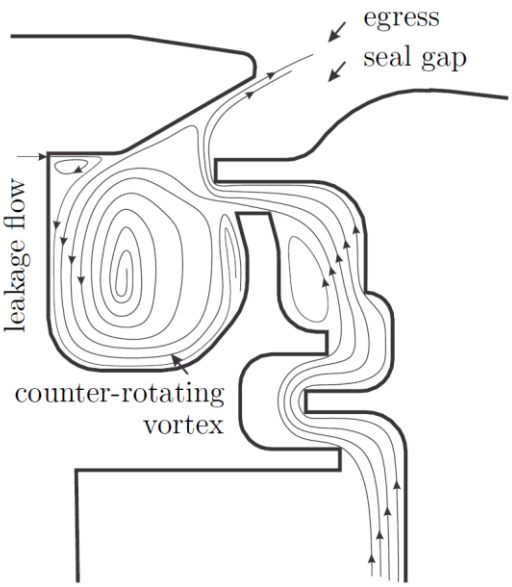
egress
seal gap
leakage flow
counter-rotating
vortex

(a)

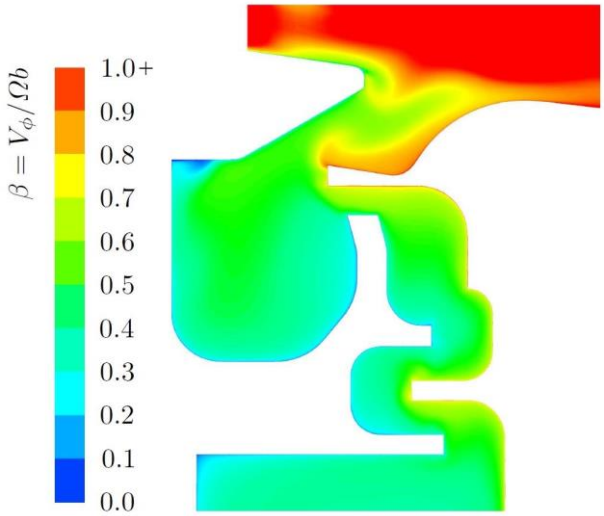
$\beta = V_\phi/\Omega b$
1.0+
0.9
0.8
0.7
0.6
0.5
0.4
0.3
0.2
0.1
0.0

(b)

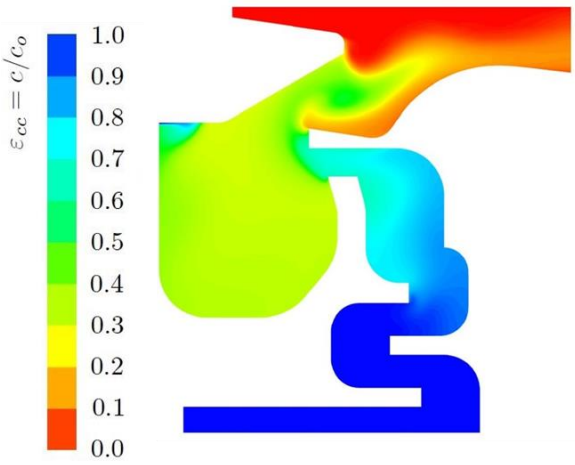
$\varepsilon_{cc} = c/c_o$
1.0
0.9
0.8
0.7
0.6
0.5
0.4
0.3
0.2
0.1
0.0

(c)

Fig. 7: Case of maximum egress for improved seal design; (a) computed velocity stream lines; (b) contour plot with swirl ratio β – note, the swirl contours were limited to $\beta = 1$ despite $\beta > 1$ in the annulus; (c) contour plot of sealing effectiveness ε_{cc}

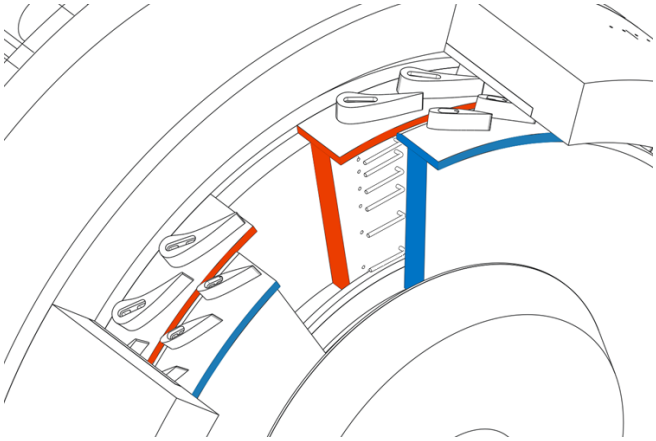

Fig. 8: Rig test section highlighting pressure instrumentation (red, stationary; blue, rotating)

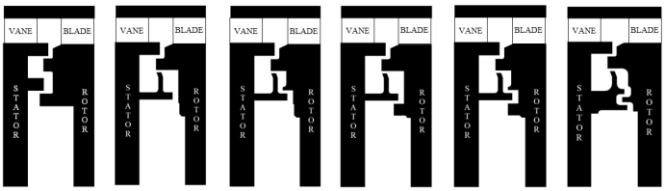

(a) (b) (c) (d) (e) (f)

Fig. 9: Evolution of rim seal design from reference seal to angel wing

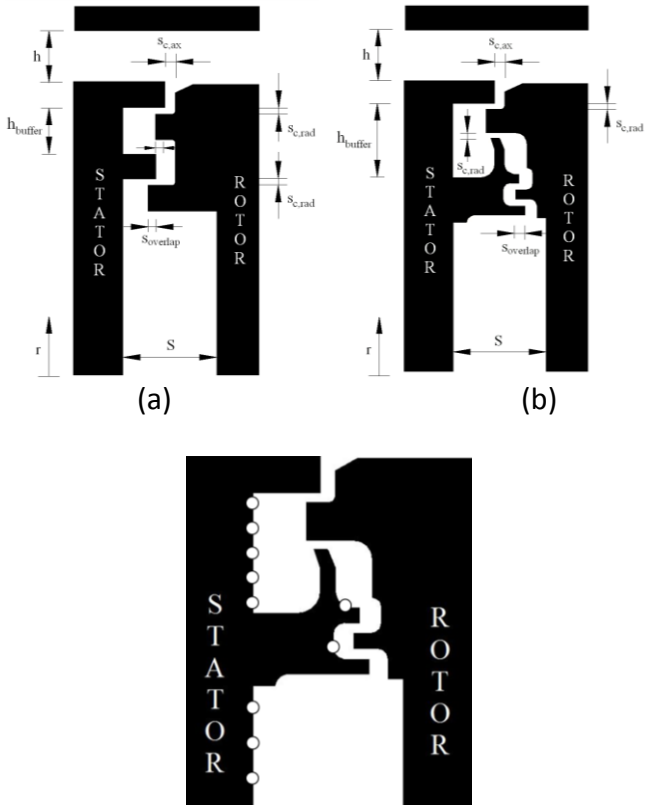

Fig. 10: (a) Reference rim seal; (b) angel-wing seal;
(c) close up of angel-wing seal showing a selection of the 15 radial measurement locations including two sampling taps within the angel-wing structure.

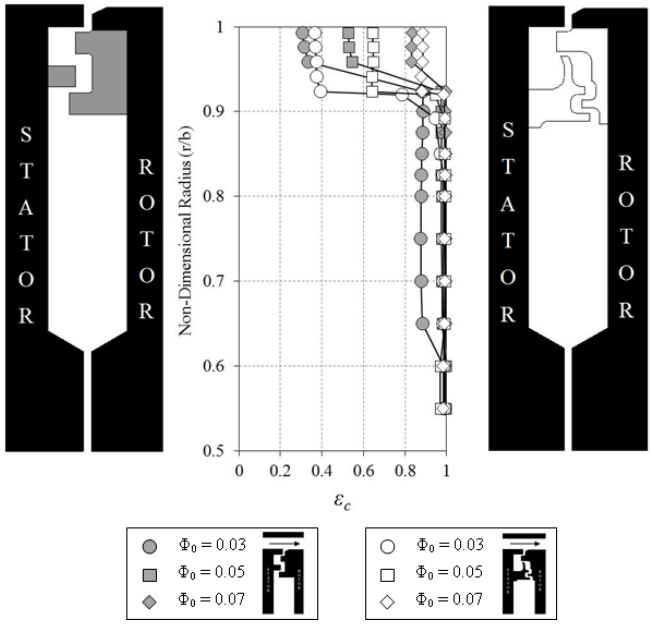

Fig. 11: Radial distribution of concentration effectiveness for reference and angel-wing seals at three sealing flow-rates

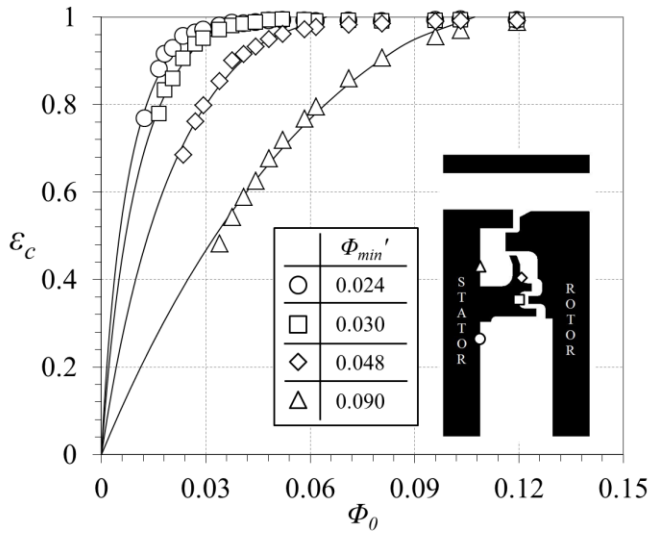

Fig. 12: Measured variation of concentration effectiveness with non-dimensional sealing flow-rate for angel-wing seal at four sampling points (Symbols denote data; lines are theoretical curves)

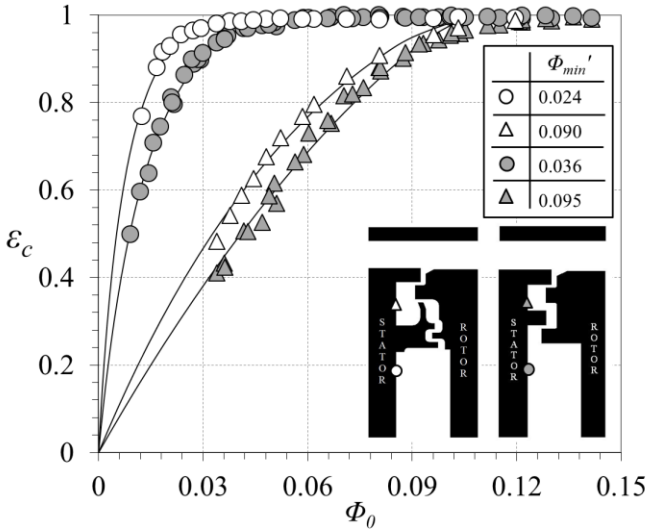

Fig. 13: Experimental variation of concentration effectiveness with non-dimensional sealing flow-rate for reference and angel-wing seals, tested at the range of conditions given in Table 1 (Symbols denote data; lines are theoretical curves)

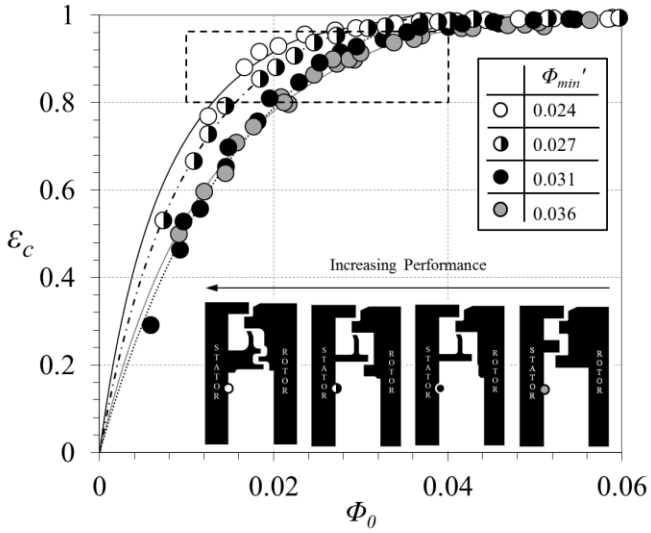

Fig. 14(a): Experimental variation of concentration effectiveness with non-dimensional sealing flow rate for four seal configurations

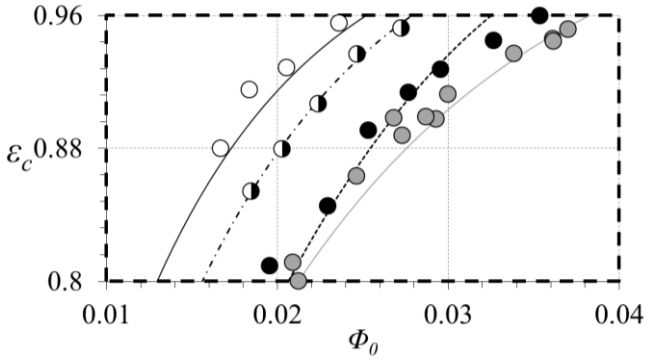

Fig. 14(b): Detail of highlighted region in Fig. 14(a)

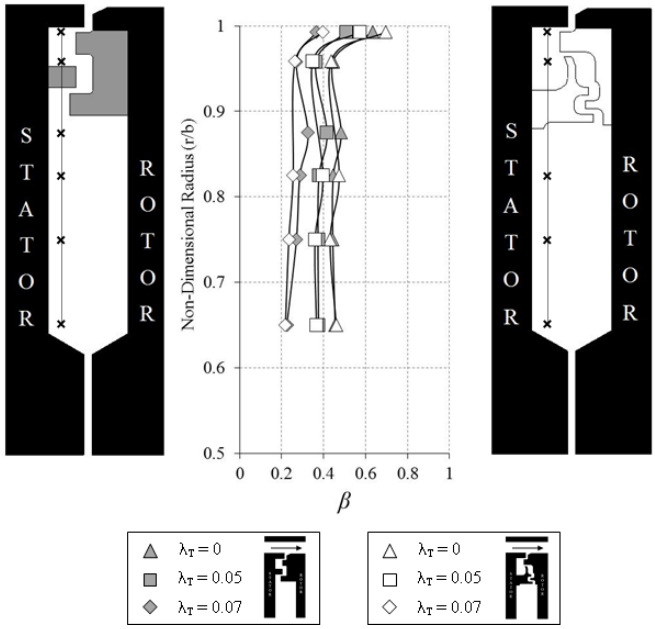

Fig. 15: Radial distribution of swirl ratio for reference and angel-wing seals at three sealant flow-rates

Table Caption List

Parameter	Disc Speed (RPM)		
	2000	3000	3500
Re_{ϕ}	5.32×10^5	8.17×10^5	9.68×10^5
Re_w	2.86×10^5	4.40×10^5	5.21×10^5
C_F	0.538	0.538	0.538
M	0.225	0.339	0.398

Table 1 Parameters for experiments

Geometric Symbol	Seal Configuration	
	Reference	Angel-Wing
h	10.0	
b	190	
S	20.0	
$s_{c,ax}$	2.00	
$s_{c,rad}$	1.28	
$s_{overlap}$	1.86	2
h_{buffer}	10	15.9

Table 2 Geometric dimensions of seal configurations (measured in mm under static conditions)